Laser-induced fluorescence spectroscopy on xenon atoms and ions in the magnetic nozzle of a helicon plasma thruster

Alfio Vinci, Stéphane Mazouffre, Víctor Gómez, Pablo Fajardo, Jaume Navarro-Cavallé

Plasma Sources Science and Technology

Laser-induced fluorescence spectroscopy on xenon atoms and ions in the magnetic nozzle of a Helicon plasma thruster

To cite this article before publication: Alfio Emanuele Vinci *et al* 2022 *Plasma Sources Sci. Technol.* in press https://doi.org/10.1088/1361-6595/ac8db8

Laser-induced fluorescence spectroscopy on xenon atoms and ions in the magnetic nozzle of a Helicon plasma thruster

Alfio E Vinci[1], Stéphane Mazouffre[1], Víctor Gómez[2], Pablo Fajardo[2] and Jaume Navarro-Cavallé[2]

[1]Institut de Combustion, Aérothermique, Réactivité et Environnement, Centre National de la Recherche Scientifique, 1C Avenue de la Recherche Scientifique, 45071 Orléans, France
[2]Equipo de Propulsión Espacial y Plasmas, Universidad Carlos III de Madrid Avenida de la Universidad 30, 28911 Leganés, Spain

E-mail: alfio.vinci@cnrs-orleans.fr,stephane.mazouffre@cnrs-orleans.fr, victor.g.garcia@alumnos.uc3m.es, pfajardo@ing.uc3m.es, janavarr@ing.uc3m.es

18 July 2022

Abstract. The dynamics of xenon atoms and ions expanding in the magnetic nozzle of a Helicon plasma thruster is studied by means of near-infrared laser-induced fluorescence spectroscopy on resonant and metastable states. Fluorescence spectra are measured for several operating conditions inside and outside the thruster discharge chamber. In the near-field plume, the relatively intense magnetic field induces Zeeman effect on the probed optical transitions. Hence, modeling of the atomic lineshapes is addressed to accurately compute the Doppler shift and infer the velocity. The first direct measurements of the neutral flow in a magnetic nozzle reveal that atoms are accelerated to supersonic velocities behind the thruster exit. The ions acceleration region extends several centimeters downstream the exit plane. Larger axial ion speeds are attained when the thruster operates at lower mass flow rates and higher levels of input power.

Keywords: magnetic nozzle, laser-induced fluorescence, Helicon, electric propulsion

Submitted to: *Plasma Sources Sci. Technol.*

1. Introduction

Research and development of electrodeless plasma thrusters currently identifies an area of interest in the electric propulsion sector [1–8]. This stems from an increasing portion of small spacecrafts being equipped with in-space maneuvering capabilities [9] which leads to the demand of alternative electric propulsion technologies. Most of the investigated kind of electrodeless devices integrate a magnetic nozzle (MN) to increase the momentum of the ejected ions thus to enhance the attained performance [10]. The use of an electrodeless discharge and MN acceleration can introduce a number of advantages over the well consolidated systems, such as Gridded Ion thrusters and Hall thrusters [11]. Any electrodeless discharge is intrinsically current-free on the full scale, therefore no neutralizer is required. Furthermore, chemical compatibility of the thruster constituents does not represent a limiting factor for the exploitation of virtually any alternative propellant.

The Helicon plasma thruster (HPT) exemplifies one of the investigated electrodeless systems. In general terms, it comprises *i*) a dielectric chamber as the plasma discharge region, *ii*) a radio-frequency (rf) antenna as the source of the input power and *iii*) an applied magnetic field having two roles: *a*) to reduce the plasma-wall interaction and enhance the plasma-wave coupling efficiency within the source, *b*) to shape a divergent MN in the external region, which is the main driver for plasma acceleration and electromagnetic thrust production. The rf power fed to the antenna allows exciting specific electromagnetic modes which mainly depend on the antenna size and geometry. The energy is coupled to the electron population as thermal energy through Helicon wave modes [12] and Trivelpiece-Gould wave modes [13]. The electromagnetic excitation is responsible for ionization and transport phenomena of the charged species, such as ambipolar electric field [14] and diamagnetic electron drift [15], eventually leading to supersonic ion velocities in the MN.

Considering that the overall maturity of this technology is relatively low [16], HPTs are currently studied by many laboratories at prototype level [17–21]. Thus far, thrust efficiency measurements do not exceed 10 % in many tested devices [6, 18, 18, 22–25], with the only exception of nearly 20 % in the high-power regime [21]. In such a scenario, the experimental approach is the preferred way to provide a deeper insight on the physical phenomena occurring throughout the MN thus suggesting strategies to performance improvement. The availability of accurate experimental data is critical for the advance in modeling of MN plasma dynamics and thruster design iteration. Under the typical conditions in terms of power levels and size ranges, ionization cost and wall losses may not represent the only primary source of inefficiency [26]. Given the low input power, the resulting low ionization fraction translates into a dense population of neutrals that inherently impacts the dynamics of the ions to be accelerated. Hence, it is clear that information about the ions and atoms velocity in the MN under different operating conditions, namely power and mass flow rate, is of crucial importance in order to assist the development and validation of more sophisticated kinetic/fluid models [27]. The currently available datasets are limited to a few studies performed on inductive plasma [26] and electron cyclotron resonance (ECR) [3, 28] thrusters. Moreover, to the best of the authors knowledge, the velocity profile of neutrals has never been reported in the literature so far.

To this end, the present paper reports on the velocity of ions and neutrals in the MN of a HPT. Measurements are performed by means of near-infrared laser-induced fluorescence (LIF) spectroscopy on resonant and metastable states. They are spatially resolved from the inside of the discharge chamber up to the far-field plume. In the proximity of the thruster exit plane, the intense magnetic field leads to a visible Zeeman effect that manifests as a relatively complex fluorescence lineshape. Accurate estimation of the Doppler shift in this region required a full modeling of the atomic line profile by accounting for all broadening mechanisms. This strategy is proposed as the unique method to infer the most probable velocity where the magnetic field strength causes the Zeeman splitting of the probed transitions. A detailed description of the experimental arrangement is provided in Section 2, which includes the HPT, the vacuum facility and the optical setup. Experimental results are presented and discussed in Section 3. Fluorescence spectra are introduced first in Section 3.1, showing the need of modeling the atomic line profile. Details of the model are then addressed in Section 3.2 and eventually theoretical and experimental lineshapes are compared to compute the Doppler shift. The resulting velocity profiles of ions and atoms are reported in Section 3.3 for a set of operating conditions. Finally, conclusions are drawn in Section 4.

2. Experimental arrangement

2.1. Thruster unit and test facility

The thruster unit (TU) tested in this work derives from a previous prototype, whose main features were described in [18]. In the current version, the magnetic field generator has been upgraded from a solenoid-based solution to an assembly of radially polarized Neodymium permanent magnets (PM). These are

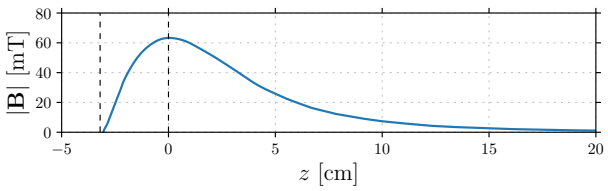

Figure 1. Axial profile of the HPT magnetic field strength. $z = 0$ refers to the exit plane of the discharge tube. The dashed vertical lines indicate the axial location of the null field and the maximum intensity which occurs at $z = 0$.

allocated in an auxiliary annular aluminum structure, which allows for a wide flexibility on the PMs configuration, thus enabling the generation of different magnetic field topologies/strengths. In this work, the PMs are assembled to form an annular ring. Since the PMs are radially polarized, they generate a symmetric magnetic field with respect to the mid-plane of the assembly, perpendicular to the z axis in Figure 2. As a consequence, the PMs mid-plane represents a magnetic separatrix surface. A null field point appears at the center of the assembly. Downstream the separatrix plane, the shape of the magnetic field is convergent-divergent, thus forming the so called MN. Upstream the separatrix plane, the field resembles the same topology because of the mentioned symmetry. The width of the PM annular assembly is 40 mm and the internal radius is 50 mm. Figure 1 shows the magnetic field strength at the centerline of the thruster in the region of interest for the LIF analysis, i.e. the exhausted plasma plume region. The peak of the magnetic field reads ≈ 65 mT and coincides with the outlet section of the plasma discharge chamber, also referred to as discharge tube within this paper. The latter is made of boron nitride, it is 60 mm long (outlet to injector plate distance), 25 mm in inner diameter and its wall thickness is 1.5 mm. The exit plane of the discharge tube is set as the reference $z = 0$ hereafter. The magnetic separatrix mentioned beforehand is placed at 40 mm upstream the tube outlet. A schematics of the thruster unit is reported in Figure 2.

Radio-frequency power at 13.56 MHz is fed to the TU through a half-helical silver coated antenna, wrapped around the ceramic tube without entering in physical contact. The antenna is 45 mm long and it has a mid diameter of 30 mm. The RF power (P_{rf}) is generated with an industrial power amplifier Seren HR2100 and it is conditioned to the antenna with a Sener Aeroespacial S.A. customized L-type matching network and control system [29]. The system can be operated up to 600 W but in this work it has been limited to lower levels.

Xenon gas is injected from the back side of

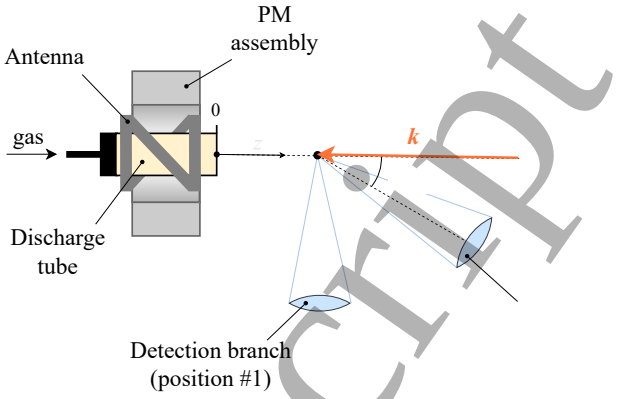

Figure 2. Experimental setup schematics. The exit plane of the discharge tube is set as the reference $z = 0$.

the tube through an embedded multi-hole injector, also made in boron nitride, which allows a uniform distribution of the propellant. The mass flow rate is set/measured by a Bronkhorst EL-FLOW Select Xenon calibrated mass flow controller, with an accuracy of 0.1 sccm and 100 sccm full range.

The thruster unit has been tested inside the main vacuum chamber of the UC3M laboratory. It consists of a non-magnetic stainless-steel vessel of 1.5 m inner diameter and 3.5 m long. The facility background pressure is about 10^{-7} mbar, while the operating pressure is kept within the range 5.9×10^{-6}–4.6×10^{-5} mbar for a Xe flow of 5 to 50 sccm. The vacuum technology implemented in the chamber consists of three cryopanels (COOLPOWER 140 T-V cryoheads by Leybold) and a couple of turbomolelucar pumps, MAG2.200iP by Leybold. The thruster axis is aligned with the vacuum chamber axis, and the thruster outlet section is about 2.5 m away from the chamber downstream wall to minimize plume-chamber wall interactions.

2.2. Optical setup

The determination of atoms and ions velocity is enabled by LIF spectroscopy. Previous works [33, 35] extensively describe this technique and the laser bench used in this study. Excitation of the probed species

Table 1. Xe I and Xe II probed optical transitions [30–34].

	Transition	λ_{exc} (air)	λ_{fluo} (air)
Xe I	$5p^5(^2P^\circ_{1/2})6s\ ^2[1/2]^\circ_1 \rightarrow$ $\rightarrow 5p^5(^2P^\circ_{1/2})6p\ ^2[3/2]_2$	834.682 17 nm	473.41 nm
Xe II	$5p^4(^3P_2)5d\ ^2[4]_{7/2} \rightarrow$ $\rightarrow 5p^4(^3P_2)6p\ ^2[3]^\circ_{5/2}$	834.724 nm	541.91 nm

is achieved via injection of a laser beam produced by an amplified tunable single-mode laser diode by TOPTICA Photonics AG in the near-infrared spectral range. The laser diode can deliver up to 600 mW in the $810-840$ nm wavelength range. In the actual experiment, the laser remains mod-hop free over a frequency tuning range larger than 5 GHz. The primary laser beam is split into multiple beams to: *i*) monitor continuously the laser mode and detect any mode hop by means of a Fabry-Pérot interferometer; *ii*) accurately measure the laser wavelength by way of a calibrated wavemeter whose absolute accuracy is 80 MHz ($\approx 60\,\mathrm{m\,s^{-1}}$). Modulation of the laser beam is achieved using a mechanical chopper at ~ 1.9 kHz.

The laser is coupled to a 50 µm optical fiber which allows transporting the beam from the optical bench to the inside of the vacuum chamber. Here the laser beam is shone through a custom collimator towards the exit of the HPT in the direction of the thruster axis, z in Figure 2. At the output of the collimator, the laser beam diameter is about 4 mm (it remains constant in the probed region), whereas the power density is typically set to $\sim 1.5\ \mathrm{mW\,mm^{-2}}$, which ensures a weak saturation effect. Note that $\mathbf{k}\cdot\mathbf{v}<0$ here, where $\mathbf{k}$ is the laser wavevector and $\mathbf{v}$ the particle velocity. The collimator is kept at a safe distance from the thruster exit plane in order to minimize plume perturbations and avoid overheating. The setup includes a detection branch which features a bi-convex lens with 60 mm focal length focusing on a 200 µm core diameter optical fiber. Due to line-of-sight constraints, the detection branch is placed perpendicularly to the laser beam when the measurements are resolved along $z>0$ (i.e. behind the thruster exit plane) and along the angular direction, whereas it is tilted by 35 deg when scanning at $z<0$. The setup configuration is shown in Figure 2. Both the excitation and detection branches are mechanically linked to a two-axes polar translation stage, whose radial and angular resolutions are 1 mm and 1 deg, respectively. Any relative displacement between the two optical branches is inhibited. The setup is arranged in such a way that the pivot point of the rotating system corresponds to the center of the thruster exit plane. The pivot point corresponds to the radial coordinate origin $r=0$. The thruster axis z is aligned with r when $\alpha=0$. It is worth remarking that, since the probed particle velocity corresponds to the component along the direction of $\mathbf{k}$, the outputs of the angular scans refer to the velocity perpendicular to the arc defined by the rotation system. The 200 µm optical fiber transports the fluorescence light to a monochromator which isolates the desired line from the whole spectrum. Afterwards, a photomultiplier tube is used to convert the light signal into voltage, which is fed into a lock-in amplifier operating at the laser modulation frequency to distinguish the signal from the natural plasma emission. A signal deconvolution is not performed in obtaining the lineshapes.

The probed optical transitions are reported in Table 1, together with the excitation and fluorescence wavelengths [30–34]. Xenon atoms are probed in the $6s\ ^2[1/2]^\circ$ resonant level, whereas xenon ions are probed in the $5d\ ^2[4]_{7/2}$ metastable level. It is worth mentioning that the LIF signals relative to atoms and ions are collected from distinct frequency tuning scans.

3. Results and discussion

3.1. Experimental results

In this section, the recorded LIF spectra are shown as a function of the laser wavelength λ. The density of Xe atoms in the probed resonant state is low due to its short lifetime [31]. As a consequence, the fluorescence signal is rapidly lost downstream the thruster exit plane, therefore the atoms profiles could only be resolved inside the discharge tube and in the near-field region of the plasma plume. Differently, the behavior of Xe ions could be investigated up to 15 cm downstream the exit plane, at the expense of longer integration times to increase the signal-to-noise ratio. The longest time required to scan over one entire profile is in the order of 8 min. The fluorescence profiles measured at large axial locations have been smoothed using a Savitzky-Golay filter.

The LIF spectra recorded for the Xe atom are shown in Figure 3 for two values of the propellant mass flow rate. It is found that the profiles exhibit a double-peak shape in the region $-2 \lesssim z \lesssim 4.5$ cm. The gap between the two peaks is maximum at $z=0$, it decreases with z and eventually the peaks merge completely behind the thruster exit plane at $z \simeq 5$ cm.

Figure 4 and Figure 5 report the Xe^+ LIF spectra recorded for several values of propellant mass flow rate and rf power, respectively. As discussed for the atoms, a double-peak lineshape is likewise observed also in this case in the region close to $z=0$, i.e. where the magnetic field strength is maximum. In the Xe^+ profiles, the two peaks merge at $z \cong 3$ cm and farther downstream the lineshape becomes almost Gaussian, cf. Figure 5. With reference to the profiles measured far downstream, it follows that either a lower propellant mass flow rate or a higher input power increases the shift of the Gaussian centerline with respect to the zero-velocity wavelength. This allows anticipating that a larger axial ion velocity is expected when the HPT is operated at lower mass flow rates and higher levels of rf power.

LIF spectra on Xe^+ are also resolved along the angular direction α, which is defined in Figure 2.

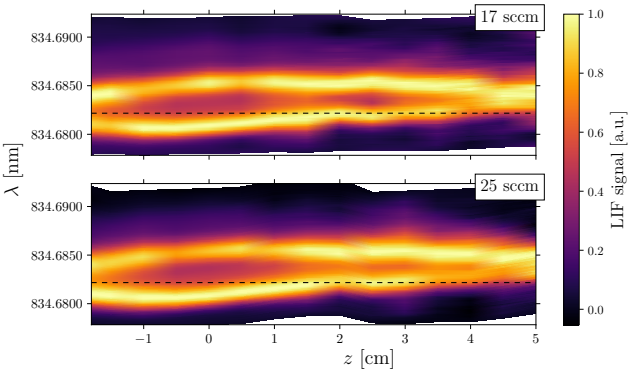

Figure 3. On-axis LIF spectra of Xe I resolved along z. The horizontal dashed line indicates the zero-velocity wavelength, cf. Table 1. Thruster operation parameters are: $P_{rf} = 350$ W, (top) $\dot{m} = 17$ sccm and (bottom) 25 sccm.

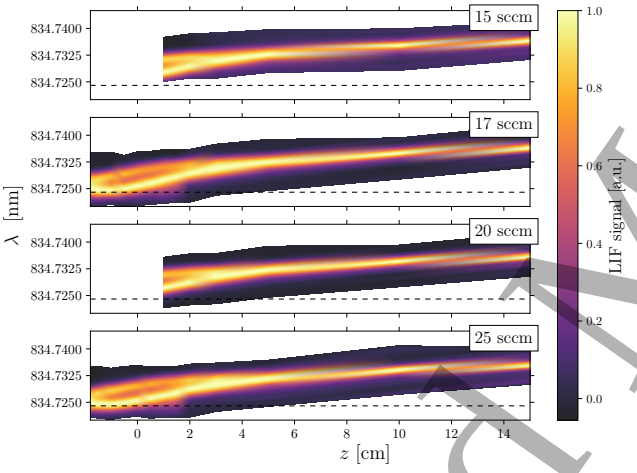

Figure 4. On-axis LIF spectra of Xe II resolved along z. The horizontal dashed line indicates the zero-velocity wavelength, cf. Table 1. Thruster operation parameters are: $P_{rf} = 350$ W, $\dot{m} = 15$ sccm, 17 sccm, 20 sccm and 25 sccm (from top to bottom).

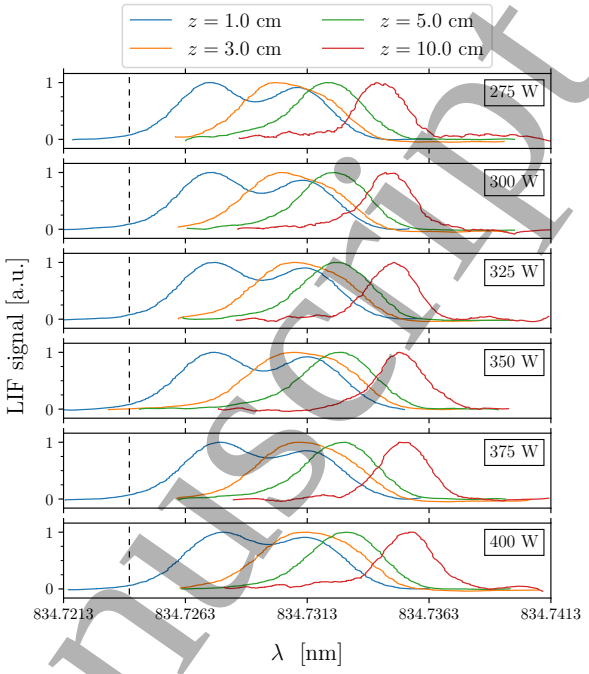

Figure 5. On-axis LIF spectra of Xe II resolved along z. The vertical dashed line indicates the zero-velocity wavelength, cf. Table 1. Thruster operation parameters are: $P_{rf} = 275$ W up to 400 W (from top to bottom), $\dot{m} = 17$ sccm.

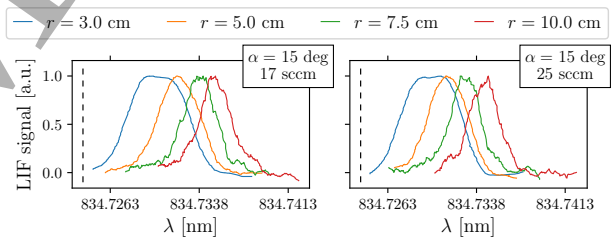

Figure 6. Examples of LIF spectra of Xe II from angular scan at $\alpha = 15$ deg for different radial distances. The vertical dashed line indicates the zero-velocity wavelength. Coordinates r and α are defined in Figure 2. Thruster operation parameters are: 350 W, (left) 17 sccm, (right) 25 sccm.

The probed region is delimited by $3 \leq r \leq 10$ cm and $0 \leq \alpha \leq 20$ deg, where r is the distance from the center of thruster exit plane. Figure 6 shows examples of fluorescence lineshapes obtained at $\alpha = 15$ deg and different radii. At $r = 3$ cm, it is observed that the two peaks almost merge resulting in a spectrum that features a plateau at its center. A larger wavelength shift occurs at larger radii, in agreement with the previous spectra related to the axial velocity. This indicates that the velocity component orthogonal to the arc along which the measurements are taken is expected to increase downstream, picturing that the ions follow trajectories divergent from the thruster center line.

Since the spectra related to both Xe and Xe^+ exhibit relatively complex lineshapes nearby the thruster exit plane, the routine assumption that they image the local velocity distribution function (VDF) cannot be applied in this case. The most probable velocity of the probed species is given by the Doppler shift of the line center. However, when the fluorescence light profile does not feature a quasi-Gaussian shape, it is not possible to identify which peak of the profile corresponds to the shifted line center, making it impossible to accurately retrieve the most probable velocity. For this reason, it is necessary to model the expected lineshape by accounting for all the possible broadening mechanisms and fit the

experimental profile thus to determine the accurate Doppler shift. Previous experiments relying on LIF have likewise observed a broadening of the recorded spectra, suggesting it was linked either to the Zeeman effect or to charge-exchange (CEX) collisions [3]. The occurrence of a population of slow ions resulting from CEX collisions cannot clarify the profiles recorded in this experiment. In fact, this hypothesis would not provide an explanation for the two peaks in the neutrals spectra as well as for the absence of slow ions farther downstream the exit plane. In Section 3.2, modeling of the atomic line profiles is addressed, proving that the form of measured lineshapes results from the Zeeman effect.

3.2. Modeling of atomic line profiles

Xenon has seven stable isotopes with abundance above 1 % [36]. Each isotope leads to the so called isotopic shift due to mass and volume differences in the nucleus. Isotopes with odd atomic number (^{129}Xe and ^{131}Xe) possess a non-zero nuclear spin I and therefore lead to the hyperfine structure (HFS). On top of that, the Zeeman effect further splits each spectral line into several components due to the presence of a relatively strong magnetic field. As a result, the absorption line comprises several optical transitions. The spectrum is modeled either in the weak or strong field approximation. The latter corresponds to the occurrence of the Paschen-Back effect. The choice of relying either on the weak or strong field approximation depends on the local strength of the external magnetic field in the context of the hyperfine interaction [37]. It is quantitatively assessed as customary by comparing the interaction energies associated with the HFS and the magnetic field at each scanning location, i.e.

$$g_J \mu_B |\mathbf{B}|/A \ll 1 \qquad \text{weak field} \qquad (1)$$

$$g_J \mu_B |\mathbf{B}|/A \gg 1 \qquad \text{strong field} \qquad (2)$$

where g_J is the Landé g-factor, μ_B is the Bohr magneton, A is the magnetic dipole constant and $|\mathbf{B}|$ is the local magnetic field intensity. For what concerns the modeling of Xe I profiles, the weak field approximation is valid as long as the magnetic field intensity remains below ≈ 0.1 T, therefore it represents a justified assumption in the present experiment. Regarding the Xe II lines instead, distinction has to be done in function of the z-coordinate. Indeed, in the proximity of the thruster exit plane, the strong field approximation provides a more realistic picture for the ^{131}Xe lines as long as the magnetic field intensity exceeds ≈ 20 mT. In practice, the whole modeling procedure consists in:

(i) finding all the allowed optical transitions;

(ii) quantifying the associated detuning frequency;

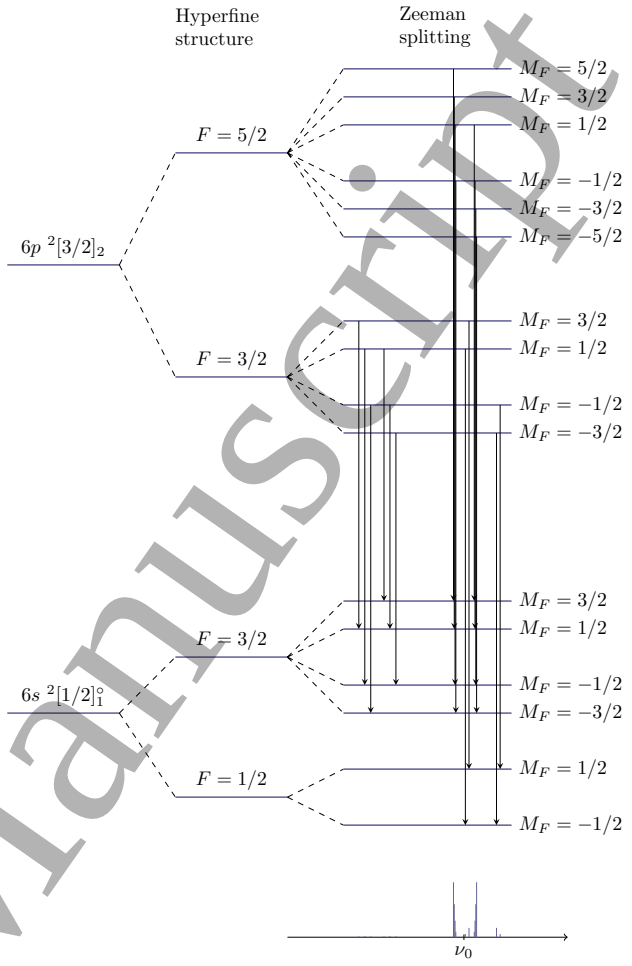

Figure 7. Instance of hyperfine and Zeeman components. Diagram relative to ^{129}Xe σ-transitions of the Xe I line at 834.682 17 nm. The lines are spaced in accordance with the computed detuning from the zero-velocity frequency ν_0 at $z = 0$. The relative intensity of each line is shown in the small graph at the base of the diagram.

(iii) determining the relative intensity of each line;

(iv) include Doppler broadening and Doppler shift to finally retrieve the lineshape.

This algorithm clearly needs to be implemented for the atoms and the ions separately.

In the weak field regime, the upper and lower energy levels of the probed transition are solved by determination of the total angular momentum F and the magnetic M_F quantum numbers for the hyperfine sub-levels, whereas the electronic angular momentum J and the magnetic M_J quantum numbers are required for the even isotopes [30, 31]. The hyperfine components are beforehand identified by the dipole-dipole selection rule $\Delta F = F - F' = [0, \pm 1]$, with $F = 0 \nrightarrow F' = 0$ [37]. In the strong field case, F and M_F are undefined quantum numbers therefore the set (I, J, M_I, M_J) needs to be used instead. The allowed

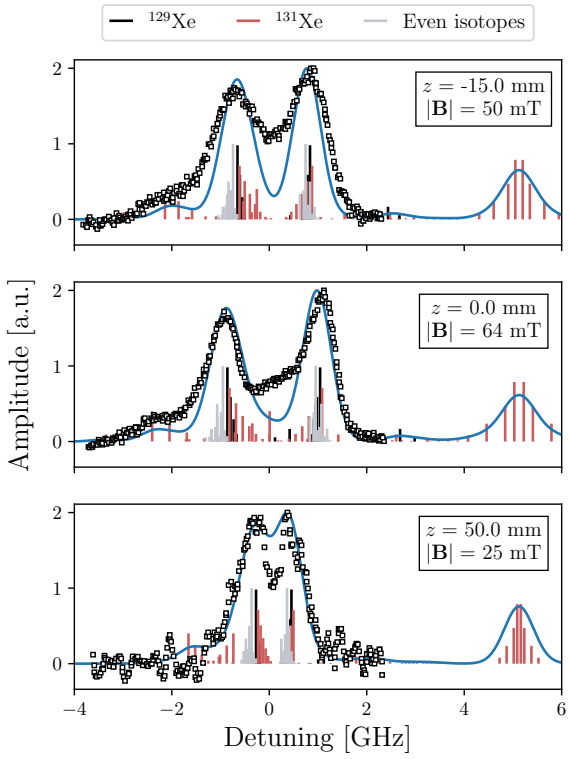

Figure 8. Experimental (squares) and modeled (line) lineshape for the $6s\ ^2[1/2]^\circ_1 \rightarrow 6p\ ^2[3/2]_2$ transition of Xe I. The experimental data points are Doppler shifted to fit the model profile. Thruster operation parameters are: 350 W, 25 sccm.

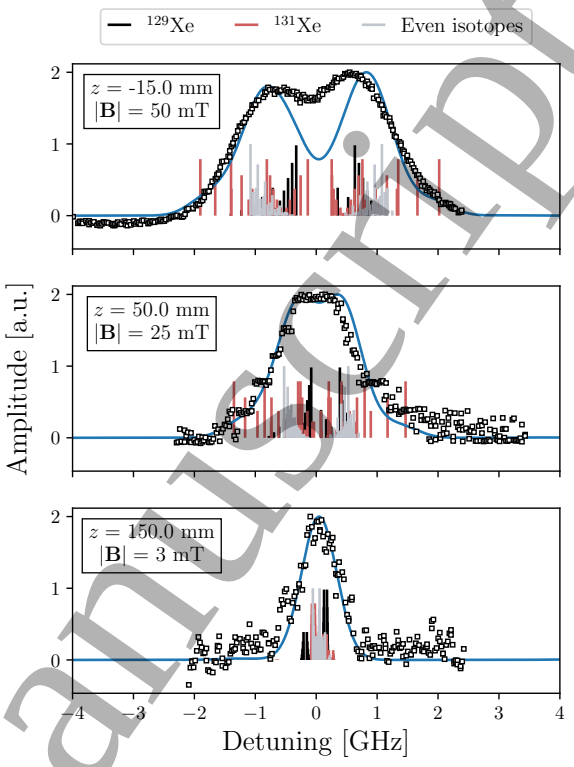

Figure 9. Experimental (squares) and modeled (line) lineshape for the $5d\ ^2[4]_{7/2} \rightarrow 6p\ ^2[3]^\circ_{5/2}$ transition of Xe II. The experimental data points are Doppler shifted to fit the model profile. Thruster operation parameters are: 350 W, 25 sccm.

transitions are set by the values of $\Delta M_{F,J}$. The latter are selected by accounting for the laser polarization with respect to the magnetic field vector. As the light at the output of the optical fiber is unpolarized, when the measurement consists in performing an axial scan, the laser is shone in the direction of the magnetic field, therefore the polarization leads to the σ components ($\Delta M_{F,J} = \pm 1$) only. Though, when the angular scans are performed, a non-null angle does exist between the laser wavenumber vector and the local magnetic field vector. In the latter case, both σ and π components ($\Delta M_{F,J} = 0$) need to be accounted for. The selection rule $\Delta M_I = 0$ is additionally considered whenever the strong field condition is met. In the simplest case when only the σ components are allowed and the weak field approximation holds, the selection rules lead to 6 lines for each even isotope, 18 for ^{129}Xe and 54 for ^{131}Xe in the $6s\ ^2[1/2]^\circ_1 \rightarrow 6p\ ^2[3/2]_2$ transition of Xe I. Regarding the $5d\ ^2[4]_{7/2} \rightarrow 6p\ ^2[3]^\circ_{5/2}$ transition of Xe II instead, the spectrum comprises 12 lines for the each even isotope, 36 for ^{129}Xe and 108 for ^{131}Xe. An instance of the allowed σ transitions due to hyperfine structure and Zeeman effect is shown in Figure 7 for ^{129}Xe isotope relative to the Xe I line at 834.682 17 nm. Several additional lines appear when the π components are included.

The energy shift of each transition is computed as the sum of three terms: the isotopic shift ΔE_{IS}, the contribution of the hyperfine structure ΔE_{hfs}, the contribution of the Zeeman effect ΔE_Z. The values of ΔE_{IS} for the Xe I and Xe II lines here investigated are tabulated in [38] and [39], respectively. It is chosen to refer these shifts to ^{132}Xe since it is the most abundant isotope. The hyperfine structure term ΔE_{hfs} is nonzero for the odd isotopes only and it is the sum of magnetic dipole and electric quadrupole contributions [30, 37, 40]. The latter are function of the hyperfine constants A and B which can be found in [30,41] for the two transitions used in this work. The last contribution to the total energy shift, i.e. ΔE_Z, is a function of the magnetic quantum number $M_{F,J,I}$, the strength of the magnetic field and the Landé g-factor g_F or g_J, depending on the isotope atomic number and weak/strong field regime. Complete expressions for ΔE_{hfs}, ΔE_Z and g_F can be found in [37]. The values of g_J and the nuclear magnetic dipole moments μ_I necessary to compute g_F are provided in [34, 42].

After the energy shift of each transition is known,

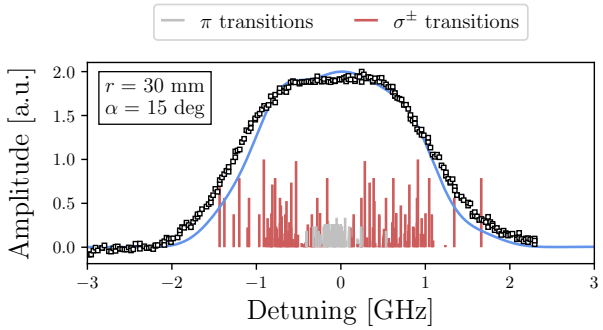

Figure 10. Experimental (squares) and modeled (line) lineshape for the $5d^2[4]_{7/2} \rightarrow 6p^2[3]^\circ_{5/2}$ transition of Xe II. The experimental data points are Doppler shifted to fit the model profile. The scan is performed at $r = 3$ cm and $\alpha = 15$ deg. Thruster operation parameters are: 350 W, 17 sccm.

the complete spectrum is built by determining the relative intensity. The equations of interest are reported in [37] for each of the π and σ components‡. They are function of F and M_F (J and M_J) for the odd (even) isotopes. The so computed intensities require to be weighted accounting for natural abundance of each isotope [36] and hyperfine components tabulated in [43] as a function of I, ΔJ and ΔF. Furthermore, in order to account for the laser polarization direction, the intensity of each π transition is scaled by $\sin(\theta)$, where θ is the local relative angle between $\mathbf{k}$ and $\mathbf{B}$. The local vector $\mathbf{B}$ is obtained from a 2-D numerical simulation which has been validated by measurements using a 3-axis gaussmeter.

At last, Doppler broadening of each transition is addressed. At this stage, two reasonable approximations are made: the laser beam profile is considered as a Dirac delta function due to its bandwidth (< 1 MHz), and the natural width (5 MHz) is neglected in comparison to the Doppler broadening full width at half maximum ($\simeq 0.65$ GHz at $T = 800$ K) [31]. It is assumed that ions and atoms share the same temperature. A Gaussian profile is applied to each component, exhibiting identical width and frequency shift. Eventually, the theoretical lineshape stems from the sum of all individual Gaussian profiles.

Figure 8 and Figure 9 illustrate two sets of the model outcomes compared to the experimental LIF spectra recorded in different locations of the plasma beam for atoms and ions, respectively. An additional comparison is provided in Figure 10 which refers to a scan performed at $\alpha = 15$ deg. The spectra in Figure 8 and Figure 9 comprise the σ transitions only as $\mathbf{k}$ and $\mathbf{B}$ are parallel, whereas the π components had to be taken into account in modeling the spectrum shown in Figure 10. A kinetic temperature of 800 K is used to fit the experimental profiles, which are Doppler shifted to overlap the model lineshape. It is observed that a portion of the Xe I spectrum has not been included in the experimental scan, cf. Figure 8. However, this fact is irrelevant considering that the focus here is on the Doppler shift. A poorly satisfactory match in the 0 GHz region is found for those profiles that exhibit a double-peak shape, for both Xe I and Xe II. In relation to this matter, the size of the laser beam and its alignment are possibly involved. For the spectra shown in Figure 8 and Figure 9, the model reasonably assumes that the excitation light is perpendicularly polarized with respect to the magnetic field. Yet, a slight misalignment and/or a relatively large probed volume would enable the occurrence of π transitions. The intensity of these transitions would be related to the angle between $\mathbf{k}$ and $\mathbf{B}$. Nevertheless, it is virtually impossible to quantify this contribution. By manually implementing a non-zero angle between $\mathbf{k}$ and $\mathbf{B}$ in the simulation code, it is found that a misalignment in the order of $2-3$ deg is sufficient to visibly alter the 0 GHz region. These values are perfectly compatible with the uncertainty associated with the experimental setup and the magnetic field simulation accuracy. Besides, it shall be mentioned that the laser is vertically polarized at the output of the diode on the optical bench. Although the multi-mode 50 µm fiber should not maintain any polarization, it may occur that a larger vertical component is preserved over the horizontal one. Given these experimental uncertainties, the goodness of fit requires a quantitative assessment. The reduced χ^2, i.e. χ^2_{red}, is herein used to estimate how well the model replicates the measured LIF profiles. Table 2 provides an overlook of the typical χ^2_{red} computed for Xe I and Xe II in three different regions of the plasma plume. These values derive from gathering all the χ^2_{red}'s associated to each measurement position for each set of thruster operating parameters (input power and mass flow rate). It is observed that a large χ^2_{red} characterizes the near-field region, whereas

‡ The results are obtained by direct substitution of $|JM_J\rangle$ and $|FM_F\rangle$ in the equations reported in [37]. The extent to which these intensities are approximations was not explored here.

Table 2. Order of magnitude of the reduced χ^2 to quantify the goodness of fit. A value $\chi^2 = 1$ indicates a good match between the model and the experimental profiles. The computed χ^2 for Xe I and Xe II accounts for all the experimental points related to Xe I and Xe II separately.

	χ^2_{red}		
	$z < 0$ mm	$0 < z < 20$ mm	$z > 20$ mm
Xe I	$\sim 10^1$	$\sim 10^0 - 10^1$	$\sim 10^0$
Xe II	$\sim 10^2$	$\sim 10^1 - 10^2$	$\sim 10^0 - 10^1$

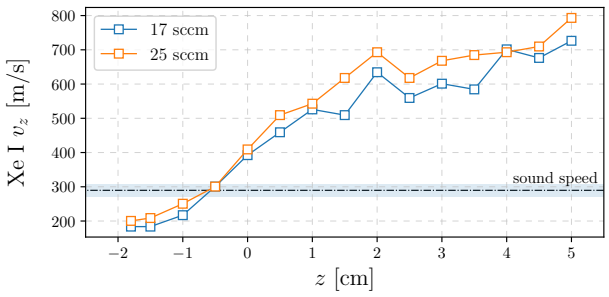

Figure 11. Axial velocity profile of Xe I for different propellant mass flow rates. Dash-dotted line indicates the sonic speed at $T = 800$ K, shaded area delimitates the ± 100 K uncertainty interval. Thruster operating parameters are: 350 W, (blue) 17 sccm, (orange) 25 sccm.

χ^2_{red} of order unity is retrieved in the far-field. Given the important effects of the magnetic field on the fluorescence lineshape near the thruster exit plane, the aforementioned experimental uncertainties lead to a poorer agreement between model and measurements. This is however of little relevance here since the main interest is to infer the most probably velocity.

In this regard, the most probable velocity is ultimately estimated from direct implementation of the Doppler shift equation [33]. This shift is equal to the off-set in the frequency axis that gives the best match between the experimental and modeled lineshapes with a precision of 10 MHz ($\approx 8\,\mathrm{m\,s^{-1}}$). This procedure is clearly embedded in the simulation algorithm. The reference zero-velocity frequency ν_0 comes from previous experiments reported in [30] relying on two-beam saturated spectroscopy in a drift-free RF plasma. Altogether, this technique allows deducing the kinetic temperature and the most probable velocity with a reasonable accuracy. The error bar results from several contributing factor, such as the uncertainty on hyperfine constants and isotopic shifts in input, the quality of the raw data, the robustness of the fitting algorithm. Although the signal-to-noise ratio decreases downstream, the single-peak shape of the recorded profiles simplifies the fitting procedure. By exploring the full range of uncertainties of the input constants to the model (i.e. isotopic shifts and hyperfine constants) and different filtering parameters on the noisy signals, it is estimated that the typical uncertainty is in the order of $\pm 10\,\mathrm{m\,s^{-1}}$ and ± 100 K for the velocity and temperature, respectively.

3.3. Velocity profiles

The velocity profiles of Xe and Xe^+ herein reported are extracted by means of the model illustrated in Section 3.2. The value of the kinetic temperature is fixed to 800 K for both species since it fits well the experimental data.

Figure 11 displays the evolution of the atoms axial velocity along the thruster center line. This data is deduced from the LIF spectra in Figure 3. It is found that the neutrals drift towards the exit plane with a velocity smaller than the thermal speed ($v_{th} = \sqrt{8k_BT_i/\pi m_i} \approx 365\,\mathrm{m\,s^{-1}}$ at 800 K). Then, the atom velocity increases within a few centimeters over the thruster exit plane up to $700 - 800\,\mathrm{m\,s^{-1}}$. Note that at 800 K and with $\gamma = 5/3$, the sound speed reads $v_s = \sqrt{\gamma k_B T_i/m_i} \approx 295\,\mathrm{m\,s^{-1}}$. Thus, the neutrals reach the sonic point in the proximity of the thruster outlet and expand supersonically within the plume. This behavior is not visibly influenced by a different value of the propellant mass flow rate. Similar upper values of the neutrals axial velocity have been found also in Hall thrusters [31]. This relatively high speed of the atoms is likely to result from various contributing phenomena. Inside the discharge chamber, the ions naturally recombine at the walls. They are reflected back with a fraction of the momentum carried before the recombination and therefore populate the high energy wing of the atoms distribution function. Ion-neutral elastic collisions may likewise contribute to increase the most probable atom velocity. The neutrals largely dominate the discharge chamber with a particle density of $\sim 10^{20}$ m^{-3}, derived from mass flow conservation and assumed uniform everywhere. As a result, the mean free path for ion-neutral momentum transfer collisions reads $\lambda \simeq 3.5$ mm using an equivalent cross section $\sigma_{el} = 2 \times 10^{-18}$ m^2 at about 1 eV of ion energy [44]. For comparison, the cross section associated with CEX collisions reads $\sigma_{CEX} \simeq 0.8 \times 10^{-18}$ m^2 [45], thus showing that elastic collisions are about 2.5 times more likely that CEX collisions. Furthermore, the slow wing of the atoms distribution function is selectively depopulated in the high electron density region, i.e. close to the magnetic nozzle throat, due to the relatively longer residence time that leads to higher ionization probability.

The profiles of the ions axial velocity are reported in Figure 12 and Figure 13 for several values of the propellant mass flow rate and input power, respectively. These profiles derive from the data shown beforehand in Figure 4 and Figure 5. For all the tested working points, it can be noticed that the ions still experience a non-negligible momentum gain several centimeters downstream the thruster exit plane. The evolution of the ion velocity at $z \lesssim 2$ cm is not visibly influenced by the thruster working condition. Indeed, all the profiles tend to merge close to the thruster exit plane. The ions leave the discharge chamber with a drift velocity of about $1.4\,\mathrm{km\,s^{-1}}$. Assuming a conservative value of the local

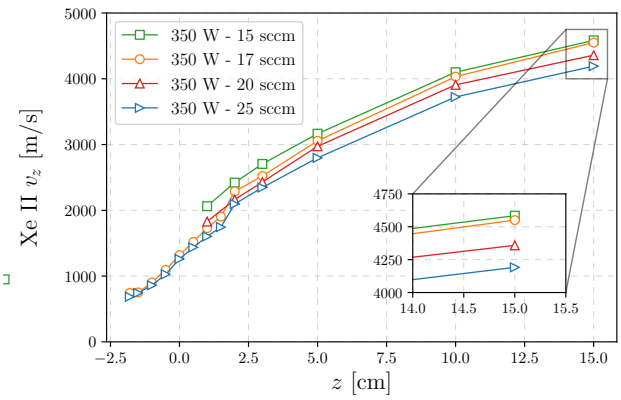

Figure 12. Axial velocity profile of Xe II for different propellant mass flow rates.

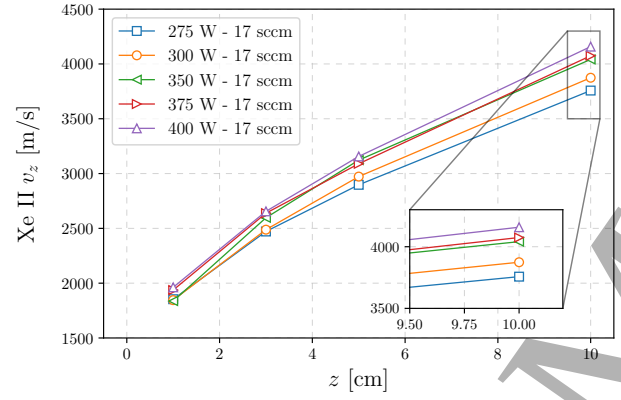

Figure 13. Axial velocity profile of Xe II for different levels of input power.

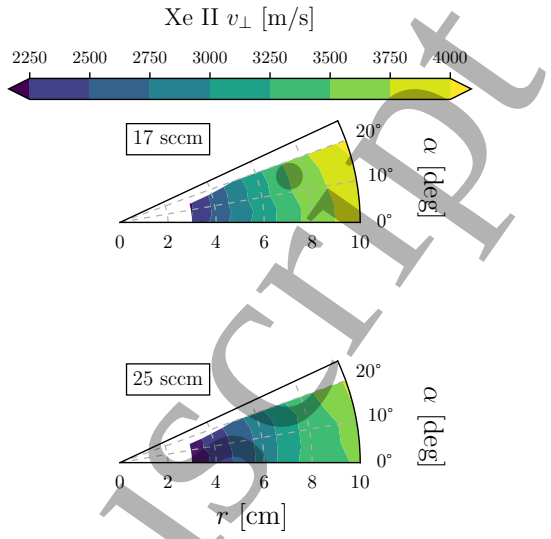

Figure 14. Contour maps of the most probable ion velocity perpendicular to the scanning arc.

electron temperature of $4-5$ eV at $z=0$ according to previous measurements taken in a similar device [18], the Bohm speed equals $1.7-1.9\,\mathrm{km\,s^{-1}}$. It clearly means that the sonic condition is reached downstream the throat of the magnetic field, in contrast with the ideal gas-dynamics analogy of the plasma expansion as routinely postulated in fluid models [14, 46]. Previous experiments in inductive and ECR thrusters [3, 26, 28, 47] have similarly observed a subsonic ion flow in correspondence of the magnetic nozzle throat. In this experiment, by accounting for positioning uncertainties in the experimental setup, the axial shift of the sonic transition is in the order of several millimeters, which is consistent with the findings reported in [3, 47]. Given that a single population of ions dominates the LIF spectra in this experiment, CEX collisions cannot explain the shifting of the sonic point. On the other hand, ion-neutral elastic collisions, electron-neutral collisions and ionization within the plume may represent a pivotal explanation to the axial shift of the sonic transition [26, 28]. The occurrence of ion-neutral collisions is compatible with the observed atom velocity profiles shown in Figure 11, as previously discussed.

The effect of a different working point of the thruster becomes more evident far downstream, cf. Figure 12 and Figure 13. A larger ultimate velocity is recorded at lower mass flow rates and higher input powers, as anticipated in Section 3.1. Altogether, the highest value of the ion axial velocity reads about $4600\,\mathrm{m\,s^{-1}}$ at $z=15$ cm, obtained for 350 W and 15 sccm.

The contour plots in Figure 14 show the most probable ion velocity related to the angular scans when the thruster operated at 17 sccm and 25 sccm. It is worth noting that the velocity in Figure 14 corresponds to the component that points in the direction identified by the angle α, see Figure 2. At small radial distances, the velocity remains nearly constant along the scanning arc. This suggests that the expanding plasma identifies a spherical surface centered at the thruster exit. Farther downstream, instead, measurements reveal that $v_\perp$ is larger at larger angles, outlining that the spherical symmetry is broken. This is also confirmed by visual inspection of the thruster during operation. Consistently with the trend of the axial velocity profiles shown in Figure 12, a lower propellant mass flow rate implies faster ions.

4. Conclusion

Xenon plasma flow velocity has been spatially resolved using laser-induced fluorescence spectroscopy in the magnetic nozzle of a Helicon plasma thruster operating under several conditions. It is found that an intense

magnetic field induces the Zeeman effect in the near-field plume, leading to a relatively complex shape of the fluorescence spectra. Consequently, it results impossible to accurately deduce the atoms and ions velocity in the strong magnetic field region without prior modeling of the atomic lineshape. Hence, this task is addressed by accounting for broadening mechanisms, namely isotopic shift, hyperfine structure and Zeeman effect. Fitting of the modeled and measured profiles allowed inferring the evolution of the most probable velocity both for the Xe atoms and ions. It is found that the neutrals axial velocity increases up to supersonic values upstream the thruster exit plane. This phenomenon is associated with parallel occurrence of several processes. The fast atoms wing of the distribution function is populated because of flow expansion, ions recombination at the walls and ion-neutral momentum transfer collisions, whereas the slow atoms wing is selectively depopulated because of ionization. The axial evolution of the ions velocity uncovers the effect of the thruster working parameters. Faster ions are obtained at lower mass flow rates and higher levels of input power. The velocity profiles also show that the acceleration region extends several centimeters downstream the exit plane. The largest velocity recorded in the probed region is about $4600\,\mathrm{m\,s^{-1}}$ at $z = 15$ cm for 350 W of input power and 15 sccm of mass flow rate.

The experimental findings reported in this paper contribute to advance in understanding the ions and atoms dynamics in a magnetic nozzle. Development and validation of numerical models can largely benefit from the data herein presented. A parallel numerical and experimental investigation of the near-field atom and ion dynamics under different working conditions would further assist in clarifying the current picture. Implementation of collisions and wall recombination phenomena in particle-in-cell models is particularly advised. It is clearly of interest to conduct a system parametric analysis targeting a larger ultimate ion velocity in view of developing an efficient electric propulsion system.

Acknowledgments

This project has received funding from the European Union's Horizon 2020 research and innovation program under grant agreement No 870542 (HelIcon PlasmA Thruster for In-space Applications). This work was also carried out in the frame of the Santander Chair of Excellence from the Carlos III University in Madrid granted to Dr. S. Mazouffre in 2020.

References

[1] Bathgate S N, Bilek M M M and McKenzie D R 2017 *Plasma Science and Technology* **19** 083001 URL https://doi.org/10.1088/2058-6272/aa71fe

[2] Takahashi K 2019 Helicon-type radiofrequency plasma thrusters and magnetic plasma nozzles *Reviews of Modern Plasma Physics* vol 3 (Springer Singapore) ISBN 0123456789 URL https://doi.org/10.1007/s41614-019-0024-2

[3] Correyero S, Jarrige J, Packan D and Ahedo E 2019 *Plasma Sources Science and Technology* **28** 095004 URL https://doi.org/10.1088/1361-6595/ab38e1

[4] Wachs B and Jorns B *Optimization of an ECR Thruster using Two Frequency and Pulsed Waveforms* URL https://arc.aiaa.org/doi/abs/10.2514/6.2021-3382

[5] Peterschmitt S and Packan D 2019 *International Electric Propulsion Conference* URL https://hal.archives-ouvertes.fr/hal-02344365

[6] Bellomo N, Magarotto M, Manente M, Trezzolani F, Mantellato R, Cappellini L, Paulon D, Selmo A, Scalzi D, Minute M, Duzzi M, Barbato A, Schiavon A, Di Fede S, Souhair N, De Carlo P, Barato F, Milza F, Toson E and Pavarin D 2021 *CEAS Space Journal* ISSN 1868-2510 URL https://doi.org/10.1007/s12567-021-00374-4

[7] Romano F, Chan Y A, Herdrich G, Traub C, Fasoulas S, Roberts P, Smith K, Edmondson S, Haigh S, Crisp N, Oiko V, Worrall S, Livadiotti S, Huyton C, Sinpetru L, Straker A, Becedas J, Domínguez R, González D, Cañas V, Sulliotti-Linner V, Hanessian V, Mølgaard A, Nielsen J, Bisgaard M, Garcia-Almiñana D, Rodriguez-Donaire S, Sureda M, Kataria D, Outlaw R, Villain R, Perez J, Conte A, Belkouchi B, Schwalber A and Heißerer B 2020 *Acta Astronautica* **176** 476–483 ISSN 0094-5765 URL https://doi.org/10.1016/j.actaastro.2020.07.008

[8] Furukawa T, Kuwahara D and Shinohara S 2021 *Physics of Plasmas* **28** 073507 URL https://doi.org/10.1063/5.0035383

[9] O'Reilly D, Herdrich G and Kavanagh D F 2021 *Aerospace* **8** ISSN 2226-4310 URL https://www.mdpi.com/2226-4310/8/1/22

[10] Takahashi K, Lafleur T, Charles C, Alexander P and Boswell R W 2011 *Phys. Rev. Lett.* **107**(23) 235001 URL https://link.aps.org/doi/10.1103/PhysRevLett.107.235001

[11] Mazouffre S 2016 *Plasma Sources Science and Technology* **25** 033002 URL https://doi.org/10.1088/0963-0252/25/3/033002

[12] Light M, Sudit I D, Chen F F and Arnush D 1995 *Physics of Plasmas* **2** 4094–4103 URL https://doi.org/10.1063/1.871032

[13] Blackwell D D, Madziwa T G, Arnush D and Chen F F 2002 *Phys. Rev. Lett.* **88**(14) 145002 URL https://link.aps.org/doi/10.1103/PhysRevLett.88.145002

[14] Ahedo E and Merino M 2010 *Physics of Plasmas* **17** 073501 URL https://doi.org/10.1063/1.3442736

[15] Takahashi K, Chiba A, Komuro A and Ando A 2016 *Plasma Sources Science and Technology* **25** 055011 URL https://doi.org/10.1088/0963-0252/25/5/055011

[16] Dale E, Jorns B and Gallimore A 2020 *Aerospace* **7** ISSN 2226-4310 URL https://www.mdpi.com/2226-4310/7/9/120

[17] Romano F, Herdrich G, Traub C, Fasoulas S, Crisp N, Edmondson S, Haigh S, Livadiotti S, Oiko V T A, Sinpetru L A, Smith K, Becedas J, Bisgaard M, Christensen S, Hanessian V, Jensen T K, Nielsen J, Sureda M, Kataria D, Belkouchi B, Conte A, Seminari S, Road O, Deimos E, Systems S and Space M 2021 Design, Set-Up, and First Ignition of the RF Helicon-based Plasma Thruster *Space Propulsion Conference 2020+1* March p 00247

[18] Navarro-Cavallé J, Wijnen M, Fajardo P and Ahedo E 2018 *Vacuum* **149** 69–73 ISSN 0042-207X URL https://doi.org/10.1016/j.vacuum.2017.11.036

[19] Shinohara S, Kuwahara D, Ishigami Y, Horita H and Nakanishi S 2020 *Review of Scientific Instruments* **91** 073507 URL https://doi.org/10.1063/5.0003387

[20] Vinci A E and Mazouffre S 2021 *Physics of Plasmas* **28** 033504 URL https://doi.org/10.1063/5.0037117

[21] Takahashi K 2021 *Scientific Reports* **11** 1–12 ISSN 20452322 URL https://doi.org/10.1038/s41598-021-82471-2

[22] Takahashi K, Lafleur T, Charles C, Alexander P, Boswell R W, Perren M, Laine R, Pottinger S, Lappas V, Harle T and Lamprou D 2011 *Applied Physics Letters* **98** 141503 URL https://doi.org/10.1063/1.3577608

[23] Pottinger S, Lappas V, Charles C and Boswell R 2011 *Journal of Physics D: Applied Physics* **44** 235201 URL https://doi.org/10.1088/0022-3727/44/23/235201

[24] Takahashi K, Charles C, Boswell R and Ando A 2013 *Journal of Physics D: Applied Physics* **46** 352001 URL https://doi.org/10.1088/0022-3727/46/35/352001

[25] Takahashi K, Takao Y and Ando A 2018 *Applied Physics Letters* **113** 034101 URL https://doi.org/10.1063/1.5041034

[26] Collard T A and Jorns B A 2019 *Plasma Sources Science and Technology* **28** 105019 URL https://doi.org/10.1088/1361-6595/ab2d7d

[27] Martinez-Sanchez M, Navarro-Cavallé J and Ahedo E 2015 *Physics of Plasmas* **22** 053501 URL https://aip.scitation.org/doi/abs/10.1063/1.4919627

[28] Wachs B and Jorns B 2020 *Plasma Sources Science and Technology* **29** 045002 URL https://doi.org/10.1088/1361-6595/ab74b6

[29] Gomez V, Giménez A, Ruiz M, Navarro-Cavallé J, Fajardo P, Wijnen M and Ahedo E 2019 RF Power - Plasma Coupling Experimental Results in a Helicon Plasma Thruster Prototype *36th International Electric Propulsion Conference* University of Vienna, Austria, September 15-20, 2019

[30] Pawelec E, Mazouffre S and Sadeghi N 2011 *Spectrochimica Acta Part B: Atomic Spectroscopy* **66** 470–475 ISSN 0584-8547 URL https://doi.org/10.1016/j.sab.2011.05.009

[31] Mazouffre S, Bourgeois G, Garrigues L and Pawelec E 2011 *Journal of Physics D: Applied Physics* **44** 105203 URL https://doi.org/10.1088/0022-3727/44/10/105203

[32] Lejeune A, Bourgeois G and Mazouffre S 2012 *Physics of Plasmas* **19** 073501 URL https://doi.org/10.1063/1.4731688

[33] Mazouffre S 2012 *Plasma Sources Science and Technology* **22** 013001 URL https://doi.org/10.1088/0963-0252/22/1/013001

[34] Kramida A, Ralchenko Y, Reader J and Team N A 2020 NIST Atomic Spectra Database (ver. 5.8), [Online]. Available: https://physics.nist.gov/asd [2021, September 16]. National Institute of Standards and Technology, Gaithersburg, MD.

[35] Mazouffre S, Kulaev V and Luna J P 2009 *Plasma Sources Science and Technology* **18** 034022 URL https://doi.org/10.1088/0963-0252/18/3/034022

[36] Sansonetti J E and Martin W C 2005 *Journal of Physical and Chemical Reference Data* **34** 1559–2259 URL https://doi.org/10.1063/1.1800011

[37] Woodgate G K 1980 *Elementary Atomic Structure* (Oxford University Press) ISBN 0-19-851146-9

[38] Suzuki M, Katoh K and Nishimiya N 2002 *Spectrochimica Acta Part A: Molecular and Biomolecular Spectroscopy* **58** 2519–2531 ISSN 1386-1425 URL https://doi.org/10.1016/S1386-1425(02)00069-0

[39] Smith T, Ngom B, Linnell J and Gallimore A *Diode Laser-Induced Fluorescence of Xenon Ion Velocity Distributions* URL https://arc.aiaa.org/doi/abs/10.2514/6.2005-4406

[40] Sargsyan A, Tonoyan A, Hakhumyan G, Leroy C, Pashayan-Leroy Y and Sarkisyan D 2015 *Optics Communications* **334** 208–213 ISSN 0030-4018 URL https://doi.org/10.1016/j.optcom.2014.08.022

[41] Broström L, Kastberg A, Lidberg J and Mannervik S 1996 *Phys. Rev. A* **53**(1) 109–112 URL https://link.aps.org/doi/10.1103/PhysRevA.53.109

[42] Fuller G H 1976 *Journal of Physical and Chemical Reference Data* **5** 835–1092 URL https://doi.org/10.1063/1.555544

[43] Kopfermann H 1958 *Nuclear Moments* (*Pure and Applied Physics* vol 2) (Elsevier) URL https://doi.org/10.1016/B978-1-4832-3061-0.50001-5

[44] Phelps database, www.lxcat.net, retrieved on September 27, 2021.

[45] Pullins S, Chiu Y H, Levandier D and Dressler R *Ion dynamics in Hall effect and ion thrusters - Xe(+) + Xe symmetric charge transfer* URL https://arc.aiaa.org/doi/abs/10.2514/6.2000-603

[46] Lafleur T 2014 *Physics of Plasmas* **21** 043507 URL https://doi.org/10.1063/1.4871727

[47] Correyero S, Jarrige J, Packan D and Ahedo E 2018 *Space Propulsion 2018, May 2018, SEVILLE, Spain* 1–8 URL https://hal.archives-ouvertes.fr/hal-01961064